



Generalized Stacking Fault Energies and Local Slip Resistances in $\text{Al}_{0.3}\text{CoCrFeNi}$: An Atomistic Study

Anshu Raj¹ · Subah Mubassira¹ · Shuozhi Xu¹

Received: 3 February 2025 / Accepted: 12 June 2025 / Published online: 23 June 2025
© The Author(s), under exclusive licence to Springer Science+Business Media, LLC 2025

Abstract

Multi-principal element alloys (MPEAs) are a type of alloy composed of multiple principal elements in near-equiatomic proportions. MPEAs are important because their complex chemistries and high configurational entropy offer enhance mechanical strength, corrosion resistance, and thermal stability, making them highly suitable for applications in extreme environments, such as aerospace and nuclear industries. This study provides a detailed examination of the $\text{Al}_{0.3}\text{CoCrFeNi}$ MPEA. Material properties, including basic structural parameters, generalized stacking fault energy (GSFE), and local slip resistance (LSR), are calculated using atomistic simulations. Pure Ni is also studied as a reference. Results reveal that the temperature dependence of the basic structural parameters in the MPEA differs from that in Ni. Additionally, the MPEA is shown to have a lower GSFE but a higher LSR than Ni. It is also observed that the LSR for the edge and screw dislocation in the MPEA is 841.73 MPa and 648.24 MPa, respectively, which is quite different from Ni, where the values are 8.5 MPa for edge dislocation and 58 MPa for screw dislocations. Furthermore, two edge dislocation insertion methods yield the same post-energy minimization dislocation structure in Ni, but not in the MPEA. Together, these findings expand our understanding of dislocation-related properties in MPEAs and emphasize the significance of appropriate atomistic model design.

Keywords Atomistic simulation · Multi-principal element alloy · Generalized stacking fault energy · Local slip resistance

Introduction

Multi-principal element alloys (MPEAs) represent a groundbreaking category of metallic materials that have attracted considerable interest in materials science and engineering due to their ability to perform well in harsh conditions, such as extreme temperatures and irradiation [1]. Unlike traditional alloys, which typically consist of a single primary element with minor additions, MPEAs are composed of multiple principal elements in equiatomic or near-equiatomic proportions [2]. This unique composition, with elements arranged in a face-centered cubic (FCC) or body-centered cubic (BCC) crystalline structure, leads to highly stable solid solutions with high configurational entropy of mixing. The pioneering work of Cantor et al. [3] and Yeh et al. [4] first demonstrated the potential of equiatomic alloys to form stable solid solutions without complex phases or

microstructures, paving the way for extensive research into MPEAs.

The investigation into MPEAs has gained momentum as they exhibit promising properties in extreme environments. Notably, MPEAs have demonstrated exceptional high-temperature strength, in some cases surpassing that of traditional superalloys, as well as remarkable resistance to irradiation, oxidation, and corrosion [5–10]. These attributes make MPEAs attractive candidates for applications that demand robust performance, such as aerospace, automotive, energy storage, defense, marine, and biomedical sectors [11, 12]. Their superior resistance to wear, oxidation, and environmental degradation highlights MPEAs as a new generation of high-performance materials with potential for transformative impact in many industry sectors [13].

A substantial body of research has focused on understanding the microstructures and mechanical properties across various MPEA systems, including $\text{Al}_x\text{CoCrFeNi}$ [14, 15], $\text{Al}_{0.3}\text{CoCrFeNi}$ [16], AlCoCuFeNi [17], AlCoCrCuFeNi [18], $\text{Al}_{0.5}\text{CoCrCuFeNi}$ [10], CoCrFeMnNi [19], AlCoCrCuFeNiSi [20], and AlCoCrCuFeMoNiTi [21]. Among these, Al–Co–Cr–Fe–Ni-based MPEAs have emerged as

✉ Shuozhi Xu
shuozhixu@ou.edu

¹ School of Aerospace and Mechanical Engineering,
University of Oklahoma, Norman 73019-1052, OK, USA

particularly promising for the development of a new class of low-density structural materials tailored for automotive and aerospace applications, where the strength-to-weight ratio is critical. These alloys have been extensively studied not only for their microstructure and mechanical performance but also for additional attributes like magnetic and electrical properties, making them versatile materials for high-demand environments [22–26].

Research shows that the mechanical properties of these MPEAs are intricately linked to the specific elemental composition and distribution within the alloy. In particular, studies on $\text{Al}_x\text{CoCrFeNi}$ alloys reveal that both the crystal structure and mechanical strength at room temperature are highly sensitive to the Al concentration [14, 22]. Variations in Al content can lead to changes in phase structure, influencing whether the alloy adopts an FCC, BCC, or mixed-phase structure, each with distinct implications for hardness, ductility, and overall mechanical performance. This sensitivity underscores the importance of precise compositional control in MPEAs to tailor their properties for specific applications.

Exploring how temperature and strain rate influence deformation mechanisms in MPEAs is vital for advancing our understanding of their mechanical behavior. Studies have shown that reducing the temperature can significantly enhance certain mechanical properties. For example, Zhang et al. [27] found that lowering the temperature from 298 to 77 K improves the yield and fracture strength of the AlCoCrFeNi MPEA, though with a reduction in ductility. Research by Gludovatz et al. [8], Gali et al. [28], and Otto et al. [29] supports that reduced temperatures improve yield strength and elongation to fracture in the CoCrFeMnNi MPEA. In contrast, Seifi et al. [30] found that increasing temperature up to 200 °C enhances the toughness of the $\text{AlCrFeNi}_2\text{Cu}$ MPEA, while Li et al. [31] reported that higher strain rates boost yield strength in the CoNiFeAlCu MPEA. Studies by Li et al. [32] shows that FCC-structured $\text{Al}_{0.1}\text{CoCrFeNi}$ MPEAs exhibit remarkable properties, with fracture strength and tensile elongation increasing from 635 MPa and 58.8% at 298 K to 1042 MPa and 81.6% at 77 K, highlighting improved strength and plasticity at lower temperatures. Similarly, Liu et al. [33] demonstrated that atomic-level heterogeneity enhances the mechanical properties of MPEAs, while another study by Liu et al. [34] showed that stacking faults in polycrystalline MPEAs further contribute to hardening through grain boundary interactions. In line with these observations, recent studies by Chen et al. [35] and Chang et al. [36] have emphasized the importance of optimizing generalized stacking fault energy (GSFE) and shear modulus to achieve a favorable balance between strength and ductility.

Despite the expanding experimental research, most studies focus on relatively macroscale behavior, leaving gaps in understanding materials at the atomic level. Atomistic

simulations [37–40] address this by offering real-time, nanoscale insights into deformation of materials, which are challenging to capture experimentally. While density functional theory (DFT) is a more accurate and reliable method, it is computationally very slow, which is why we opt to use the atomistic simulation method instead. In this study, we used atomistic simulations to calculate basic structural parameters, GSFEs, and local slip resistances (LSRs) in single-crystalline $\text{Al}_{0.3}\text{CoCrFeNi}$ MPEA, which has been experimentally confirmed to have an FCC phase [41, 42]. This alloy is selected because Chen et al. [35] confirmed its exceptional creep resistance by demonstrating that its creep strain rate is several orders of magnitude lower than that of the Cantor alloy and its derivative compositions. The effect of chemical short-range order in this alloy has been explored by Sun et al. [43] and Hasan et al. [44]. Therefore, this study focuses on analyzing the alloy in its randomized structural state. LSR is a focus here because it plays a critical role in determining mechanical performance. Pasianot et al. [45] found that in FCC CoCrCuFeNi , the LSR of the screw dislocation is higher than that of edge dislocation, with values ranging from 125 to 150 MPa for both types. The finding is similar to that in BCC MoNbTi reported by Xu et al. [46]. In contrast, a study by Nitol et al. [47] on BCC NbTiTaV and NbTiTaVZr alloys shows that the LSR associated with edge dislocation exceeds that of screw dislocation. Similarly, Romero et al. [48] found that among four BCC MPEAs, the edge LSR is higher than the screw LSR in some cases, while the opposite is true in others. It is one of our goals in this paper to clarify the relationship between the edge LSR and screw LSR in FCC $\text{Al}_{0.3}\text{CoCrFeNi}$.

Materials and Methods

Software

In this study, we use the Large-scale Atomic/Molecular Massively Parallel Simulator (LAMMPS) [49] (version 2 Aug 2023) because of its capability to manage complex, large-scale simulations with high precision. We utilized AtomsK [50] to construct crystalline structures for both MPEA and pure Ni, which is used as a reference. For the analysis and visualization of our simulation outcomes, we employed the Open Visualization Tool (OVITO) [51].

Interatomic Potential

Our simulations utilize the embedded atom method (EAM) interatomic potential, which is especially effective for studying metallic alloys as it accounts for the embedding energy of atoms. Unlike traditional pair potentials, which only consider interactions between pairs of atoms, the EAM approach

enables a richer understanding of how atoms collectively influence each other within the alloy structure.

The EAM potential energy formulation is expressed as follows [52]:

$$E = \frac{1}{2} \sum_{i=1}^N \sum_{\substack{j=1 \\ j \neq i}}^{N_{\text{nei}}} V(R^{ij}) + \sum_{i=1}^N F(\rho^i) \quad (1)$$

In this equation, N denotes the total number of atoms, while N_{nei} indicates the number of neighboring atoms surrounding atom i . V represents the pair potential, and F stands for the embedding potential. The term ρ^i signifies the host electron density at atom i . Additionally, R^{ij} is the magnitude of the vector pointing from atom i to atom j , defined as follows:

$$R^{ij} = R^j - R^i \quad (2)$$

$$\rho^i = \sum_{\substack{j=1 \\ j \neq i}}^{N_{\text{nei}}} \rho^j(R^{ij}) \quad (3)$$

Here, ρ^{ij} represents the local electron density contribution from atom j to atom i . Importantly, the definitions of V and ρ^{ij} depend solely on the type of atom i and the distance R^{ij} between atom i and its neighboring atom j , irrespective of the type of atom j .

Specifically for $\text{Al}_{0.3}\text{CoCrFeNi}$, we will primarily use the EAM potential developed by Farkas and Caro [53]. As will be shown in Section 3.3, this potential provides more reliable GSFE curves in both pure Ni and MPEA, compared to those obtained by another popular EAM potential that was developed by Zhou et al. [54]. Notably, the Farkas and Caro potential has been widely used in the literature for investigating various properties of the AlCoCrFeNi alloy family, including phase stability [55, 56], thermal stability [57, 58], vacancy deformation energy [59], and thermal expansion [44].

Lattice Parameter

We build three unique random atomistic structures for FCC $\text{Al}_{0.3}\text{CoCrFeNi}$. The simulation cell is aligned so that the [100], [010], and [001] crystallographic orientations match the x -, y -, and z -axes, respectively. Each simulation cell, with periodic boundary conditions (PBCs) applied along all three directions, contains a total of 32,000 atoms. For the lattice parameter at 0 K, each cell was gradually stretched by assuming different trial lattice parameters. For each stretched cell, the bulk energy was calculated. The actual lattice parameter, a_0 , was identified from the cell with the lowest bulk energy [60]. For the lattice parameter at finite temperatures (up to 1073 K),

we perform molecular dynamic simulations in an NPT ensemble for 10 ps, and the time-averaged lattice parameter during the last 1 ps is calculated. At any temperature, the mean value of three a_0 is reported as the final lattice parameter.

Elastic Constants

We first build simulation cells with the correct lattice parameter for $\text{Al}_{0.3}\text{CoCrFeNi}$ at different temperatures. The [100], [010], and [001] crystallographic orientations are aligned along the x -, y -, and z -axes, respectively. Each simulation cell contains 32,000 atoms and has an edge length of about 7.3 nm along each axis. At 0 K, the stiffness tensor is computed using the stress–strain approach [61]. At finite temperatures, the elastic constants are determined using the Born matrix method [62].

At any temperature, the effective FCC elastic constants are calculated via [63]

$$\begin{aligned} C_{11}^{\dagger} &= \frac{C_{11} + C_{22} + C_{33}}{3} \\ C_{12}^{\dagger} &= \frac{C_{12} + C_{13} + C_{23}}{3} \\ C_{44}^{\dagger} &= \frac{C_{44} + C_{55} + C_{66}}{3} \end{aligned} \quad (4)$$

Generalized Stacking Fault Energy

GSFE constitutes an energy landscape that is closely related to the slip characteristics of metallic materials. In crystals, dislocations mostly glide occurs by in-plane shearing, which involves the breaking of atomic bonds in the plane. The resistance to this glide is partly governed by the GSFE. In this study, molecular statics methods are employed to calculate the GSFE at 0 K.

The simulation cell consists of 54,000 atoms. Cell dimensions are set at about 7.5 nm along the x -axis, 13 nm along the y -axis, and 6.1 nm along the z -axis. The x -, y -, and z -axes were aligned with the crystallographic directions $[1\bar{1}0]$, $[11\bar{2}]$, and $[111]$, respectively, with PBCs applied in the x - and y -directions only. To map the GSFE surface of $\text{Al}_{0.3}\text{CoCrFeNi}$, we shift the upper half of each specimen along the y -axis within the xy -plane, as shown in Fig. 1. For statistical reliability in the MPEA, GSFE surfaces are calculated across 20 distinct parallel planes, ensuring that the final results offer a robust representation of the material's property [64]. Only one plane is considered in pure Ni.

Local Slip Resistance

To thoroughly understand the plastic deformation behavior in metals, analyzing the dynamics of dislocation movement

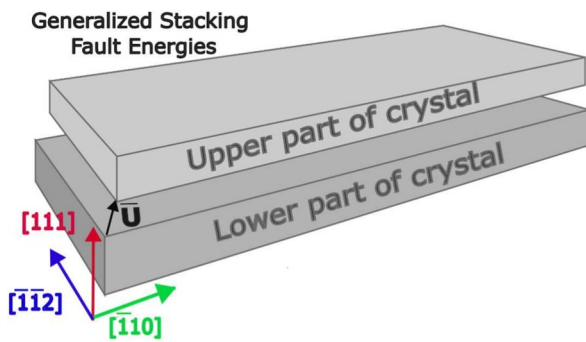


Fig. 1 A schematic of the GSFE calculation, whereas the upper and lower crystals are displaced with respect to each other along an in-plane vector \bar{U}

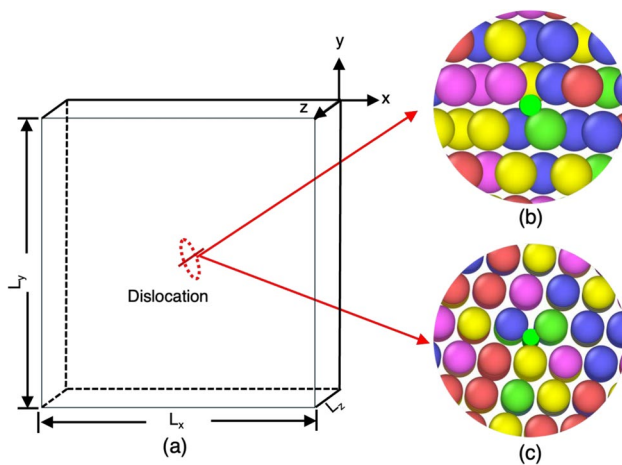


Fig. 2 a Schematic of the simulation cell for calculating the LSR of an edge or a screw dislocation in the MPEA and the Peierls stress in Ni at 0 K. Atoms in the MPEA, colored by species, around the dislocation line are shown in (b) and (c) for edge and screw dislocations, respectively

is crucial [65]. In FCC crystals, dislocations primarily glide on $\{111\}$ planes [66]. In pure metals, this gliding behavior is characterized by the Peierls stress, a threshold value of resolved shear stress required to move a dislocation through the lattice [67]. However, in MPEAs like $\text{Al}_{0.3}\text{CoCrFeNi}$, this concept is extended to what is known as the LSR, which is the minimum resolved shear stress required to move a dislocation through a chemically complex distorted lattice.

As shown in Fig. 2, the simulation framework aligns specific crystallographic directions to analyze edge and screw dislocations under controlled conditions. For edge dislocations, the $\bar{1}10$, 111 , and $11\bar{2}$ directions are mapped onto the x -, y -, and z -axes, respectively, while for screw dislocations, the orientations of $\bar{1}\bar{1}2$, 111 , and $\bar{1}10$ are used. Each simulation cell is sized at $L_x = 40$ nm, $L_y = 50$ nm, and $L_z \approx 1$ nm. The total number of atoms varies by dislocation type, with

78,966 atoms in the edge dislocation cell and 103,356 atoms in the screw dislocation cell. To capture the randomness in atomic distribution, we build 20 atomistic structures for each dislocation type.

The focus of this investigation is to calculate LSR for both edge and screw dislocations on the $\{110\}$ plane at 0 K using molecular statics. We employ the “periodic array of dislocation (PAD)” model which was found to be the most appropriate model for the Peierls stress calculation [61]. In the PAD model, PBCs are applied along the dislocation gliding direction, i.e., the x direction, and the dislocation line direction, i.e., the z -direction.

Here, the screw dislocation is inserted at the center of the simulation cell displacing atoms following the corresponding elastic displacement field [68]. However, for the edge dislocation, applying the corresponding elastic displacement field does not lead to a PAD model, specifically, the cell along the dislocation gliding direction would not be periodic. Thus, the creation of an edge dislocation is a bit more complicated. To build a PAD model containing an edge dislocation, there are three main methods [69]. The first one involves stacking two crystal blocks [70]: the top block is given an extra column of atoms and then compressed by half the Burgers vector, while the bottom block was stretched by the same amount to make their lengths along the x -axis match. To introduce the dislocation, these blocks are seamlessly merged along the y -axis, resulting in a single, continuous crystal with an edge dislocation. In the second method, an edge dislocation is introduced by deleting half-planes of atoms above or below the glide plane [71]. This causes the system to shrink along the x -axis, which is then adjusted by automatically reducing the box vector by half the Burgers vector. The third method is similar to the second one except that half-planes of atoms are added below or above the glide plane [72]. Since the last two methods are similar, we consider in this paper only the first two methods, which are denoted as “Edge1” and “Edge2,” respectively, as shown in Fig. 3.

Once a dislocated cell is built, energy minimization is applied to relax the system. It follows that a gradual shear strain 10^{-6} per step for the screw dislocation and 10^{-5} per step for the edge dislocation is applied. Energy minimization is applied after each incremental strain. We then monitor the dislocation motion across the crystal lattice until it traverses at least 1 nm. For more details on the methodology, readers are referred to our prior work [46, 48]. Eventually, a set of 20 LSR values is obtained for the MPEA. Similarly, the Peierls stress in Ni is calculated as a reference.

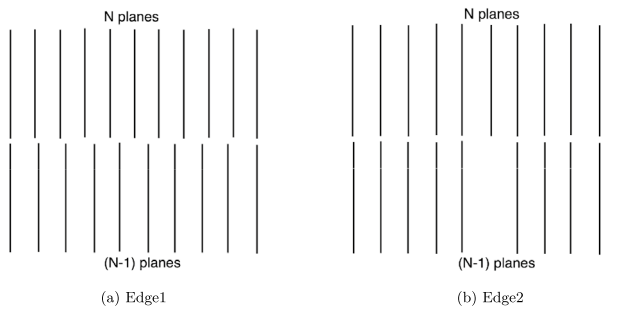


Fig. 3 Schematic illustration of the two methods employed to create an edge dislocation

Table 1 Lattice parameters a_0 of Ni and MPEA at 300 K, in Å

	Method	a_0 (Å)	Reference
Ni	EAM_Farkas	3.533	This work
	EAM_Zhou	3.533	This work
	DFT	3.516	[73]
	Exp	3.524	[74]
MPEA	EAM_Farkas	3.586 ± 0.000084	This work
	EAM_Zhou	3.618 ± 0.000032	This work
	Exp	3.57	[23]
	Exp	3.58	[43]

Note that the DFT calculation was at 0 K

Results and Discussion

Lattice Parameter

First, we calculate the lattice parameter at 300 K for both MPEA and Ni using both EAM potentials and compare

them with DFT and experimental values, as shown in Table 1. The comparison is generally good.

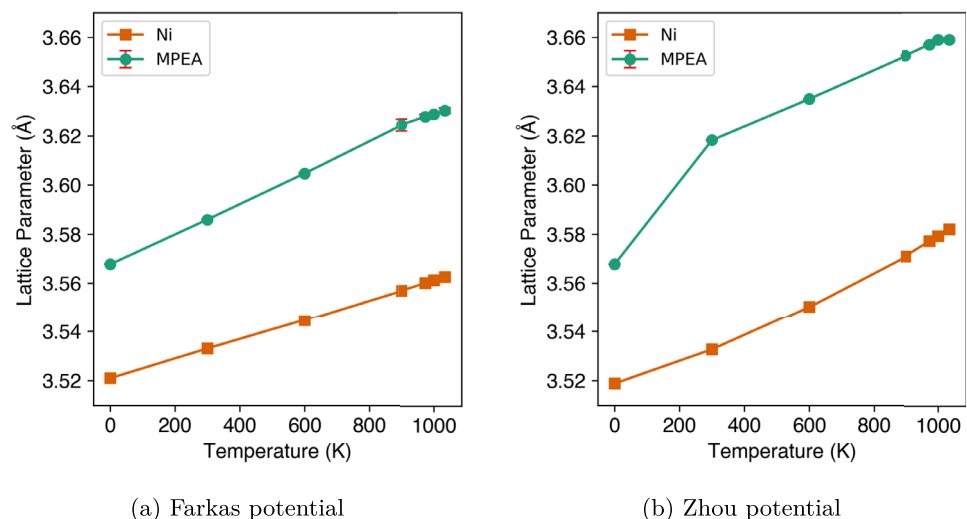
Then, Fig. 4 illustrates the relationship between temperature and lattice parameters of both MPEA and Ni. As anticipated, both materials display an upward trend in lattice parameters as the temperature increases, which is characteristic of thermal expansion. Throughout the entire temperature range, the MPEA consistently exhibits a larger lattice parameter compared to Ni. The error bars for the MPEA data represent the standard deviation from three separate measurements. Interestingly, some error bars are absent because the lattice parameter values at certain temperatures are almost identical across all measurements.

Elastic Constants

First, we calculate the elastic constants at 300 K for both MPEA and Ni using both EAM potentials and compare them with DFT and experimental values, as shown in Table 2. The comparison is generally good.

Figure 5 illustrates how the elastic constants (C_{11} , C_{12} , and C_{44}) of the MPEA and Ni depend on different temperatures. For the MPEA, we observe a steady decrease in these constants as the temperature rises. A similar pattern is observed for Ni, except that the elastic constants at 0 K are smaller than those at 300 K using the Farkas potential. This exception is not aligned with either experiments [77] or prior modeling [78], suggesting a limitation of the Farkas potential. Similar to the lattice parameter, the error bars in Fig. 5 represent the standard deviation from three measurements for the MPEA. As the temperature increases, the deviation initially increases but then decreases.

Fig. 4 Temperature dependence of the lattice parameters of Ni and MPEA using the (a) Farkas and (b) Zhou potentials



Generalized Stacking Fault Energy

The $\langle 112 \rangle$ GSFE curves for Ni and MPEA are presented in Fig. 6. Along the curve, unstable SFE (USFE) and intrinsic SFE (ISFE) are two important values within the context of GSFE analysis. It is shown that for Ni, both EAM

potentials predict ISFE and USFE generally well, with respect to the DFT data [73]. For the MPEA, however, the Farkas potential predicts the anticipated GSFE curve shape, while the Zhou potential does not. Therefore, only the Farkas potential will be used in the remainder of this paper.

Table 2 Elastic constants of MPEA and Ni at 300 K, in GPa

	Method	C_{11}	C_{12}	C_{44}	Reference
Ni	EAM_Farkas	295.563	174.239	148.675	This work
	EAM_Zhou	221.161	133.962	112.183	This work
	DFT	278.87	158.83	132.18	[73]
	Exp	247	153	122	[75]
MPEA	EAM_Farkas	220.139±1.41	142.386±0.81	116.474±1.14	This work
	EAM_Zhou	221.015±1.23	142.204±0.94	117.963±1.38	This work
	Exp	229	147	113	[76]
	Exp	221.49	136.72	117.21	[35]

Note that the DFT calculation was at 0 K

Fig. 5 Temperature dependence of the elastic constants (C_{11} , C_{12} , and C_{44}) of Ni and MPEA using the (a) Farkas and (b) Zhou potentials

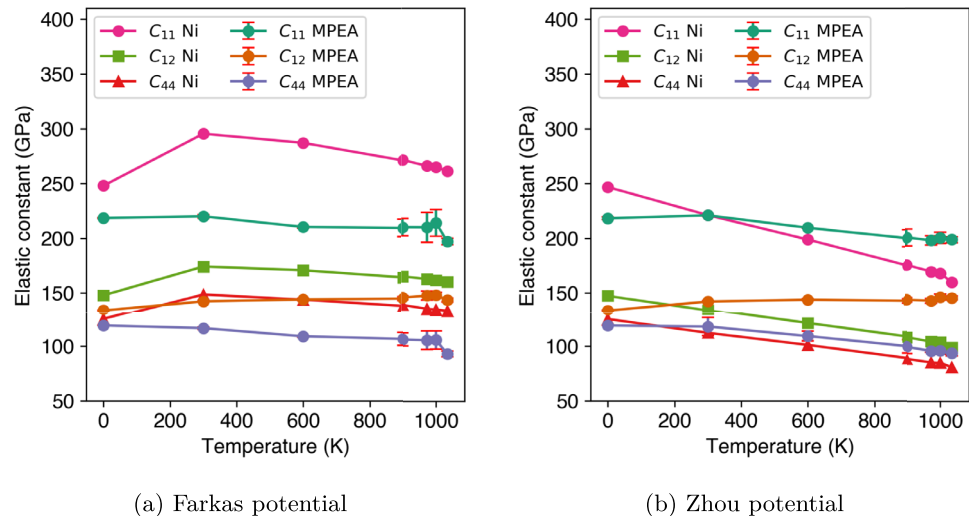
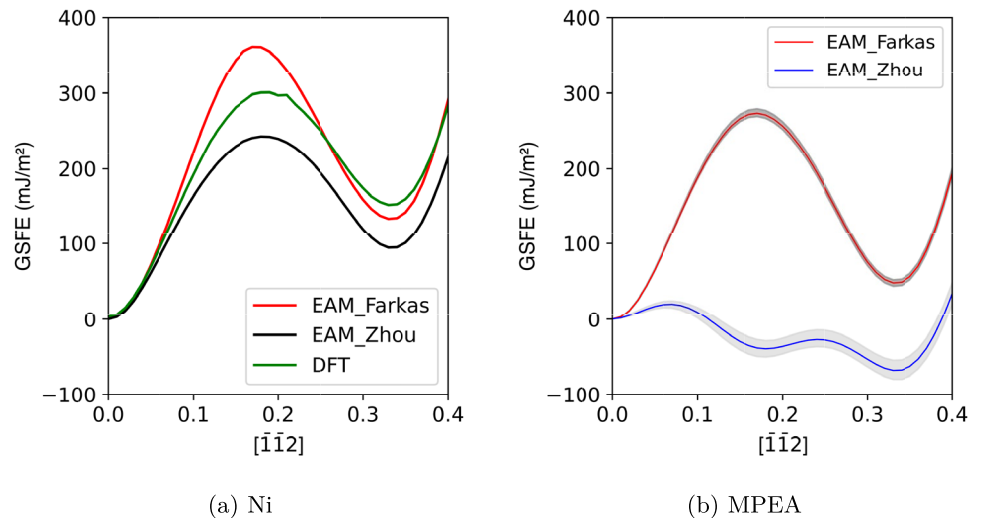


Fig. 6 GSFE curve for (a) Ni and (b) MPEA. In (a), DFT data are from Su et al. [73]. In (b), the shade represents the standard deviation of the 20 GSFE curves based on 20 different random structures



A positive ISFE is indicative of a stable FCC structure, whereas a negative ISFE suggests a transition toward a more stable hexagonal close-packed (HCP) phase. Based on the Farkas potential, it is evident from Fig. 6 that both Ni and MPEA have a stable FCC structure. The MPEA's ISFE is between 43.64 and 52.29 mJ/m² and its USFE is between 268.70 and 279.19 mJ/m². Ni, on the other hand, shows noticeably higher stacking fault energies, with the ISFE being 133.24 mJ/m² and the USFE being 361.37 mJ/m². The findings are in accordance with previous studies, which found that FCC MPEAs generally have lower GSFEs than pure FCC metals [79].

To get a clearer and more detailed understanding of the GSFE, we calculated the GSFE surface for both Ni and the MPEA using the Farkas potential, as shown in Fig. 7. In Fig. 7b, we specifically highlight the GSFE surface with the lowest ISFE among the 20 surfaces we analyzed. What is particularly noteworthy is that the shapes of the GSFE surfaces for both Ni and the MPEA are quite similar, which reinforces the accuracy and reliability of the Farkas potential. This shows that the potential is well suited for modeling GSFEs in this MPEA.

Local Slip Resistance

LSRs for both edge and screw dislocations on the {111} slip plane in MPEA are summarized in Table 3. For MPEA, the shown LSR values are the mean of 20 separate measurements. In contrast, only a single Peierls stress value is recorded for each type of dislocation in Ni, also on the {111} plane. As expected, the LSRs in the MPEA are much higher than the Peierls stress in Ni, as a result of the former's highly distorted lattice. In Ni, the edge dislocation experiences a lower Peierls stress compared to the screw dislocation, which is a typical trend in FCC metals [80]. However, this behavior is reversed in the MPEA, where edge dislocations

exhibit higher LSR than screw dislocations. In the literature, the LSR of edge and screw dislocations were found to be similar in some FCC MPEAs (e.g., CoCrCuFeNi [45]) and BCC MPEAs [47, 48, 81]. Taken together, these findings highlight the complex interactions within MPEAs, where the local atomic environment play crucial roles in influencing dislocation dynamics.

Figure 8 illustrates the distinct distribution patterns of the LSR for edge and screw dislocations in the MPEA. Edge dislocations predominantly appear in the higher LSR ranges, particularly within the 500–1000 MPa range, indicating that they face greater resistance to movement. In contrast, screw dislocations are more frequently observed in the lower LSR ranges, especially between 0–250 MPa and 500–750 MPa. This disparity in LSR distribution provides insight into the unique dislocation behavior within MPEAs, highlighting the influence on LSR by the local chemical environment.

Next, we turn our attention to the difference in LSR between two types of edge dislocations: Edge1 and Edge2. Table 3 shows that the two types of edge dislocation possess almost the same Peierls stress in Ni, but different LSRs in the MPEA. To understand the mechanism, we look into their atomistic structures. Figure 9 shows that the atomistic structures for Edge1 and Edge2 in Ni before the energy minimization differ, yet those after the energy minimization are almost the same. In other words, the two methods yield very similar minimized structures and Peierls stresses in Ni.

Table 3 Peierls stress for Ni and LSR for MPEA, in MPa

Dislocation	Ni	MPEA
Edge1	8.9	1045.742
Edge2	8.5	841.733
Screw	58	648.241

The Farkas potential is used

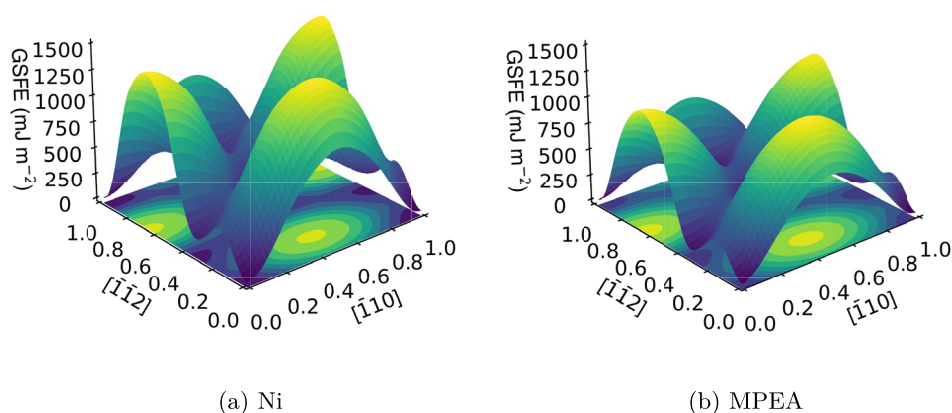


Fig. 7 GSFE surface for (a) Ni and (b) MPEA using the Farkas potential. In (b), the surface with the lowest ISFE among the 20 surfaces is shown

However, a different phenomenon is observed for the MPEA, see Fig. 10. We found that even stringent energy minimization convergence criteria fail to shorten the stacking fault width of Edge1 in the MPEA. In addition, we performed the same energy minimization using a larger simulation cell, with both L_x and L_y doubled; the same phenomenon was found for the MPEA. Attempting to further compare the two energy minimized structures in the MPEA in Fig. 10c, d, we calculate the potential energy per atom in each structure. The excess potential energy per atom, with respect to an undislocated structure, are found to differ by less than 8×10^{-5} eV between the two models. As a result, we cannot state whether Edge1 or Edge2 is more suitable based on the potential energy. That said, our opinion is that Edge2 is more suitable for the MPEA because it produces a more reasonable stacking fault width after energy minimization.

The next question is whether there is a way to shorten the stacking fault in Edge1 in the MPEA. To assess that

we perform molecular dynamic simulations to dynamically relax the as-built structure (see Fig. 10a) in the MPEA. Each simulation was run for 1 ns at different temperatures of 10 and 50 K, respectively. As shown in Fig. 11, the finite-temperature dynamic relaxation at as low as 10 K is able to shorten the stacking fault in Edge1. It also expands the stacking fault in Edge2, similar to the effect of energy minimization. Similar results were found for Edge2 in Ni (not shown here). These findings underscore the importance of selecting the optimal dislocation configuration to achieve accurate calculations of properties of MPEAs, especially in relation to dislocation resistance and movement.

Fig. 8 Distribution of 20 LSRs for edge and screw dislocations on {111} plane in the MPEA. The Farkas potential is used

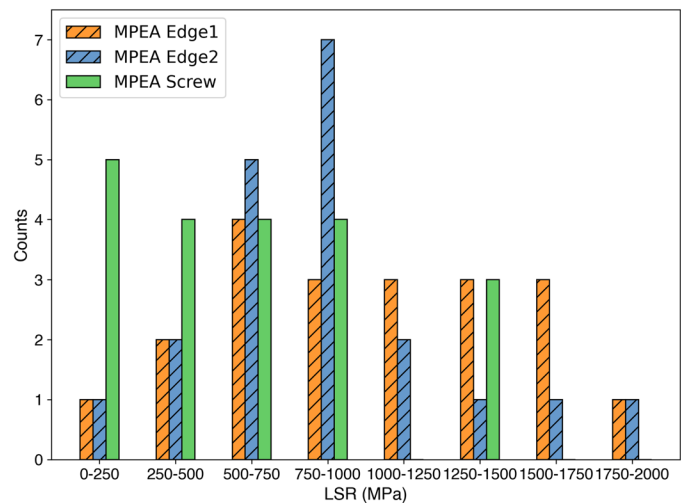


Fig. 9 Edge1 and Edge2 in Ni before and after energy minimization. Red, green, and gray atoms are those with HCP, FCC, and distorted lattices, respectively

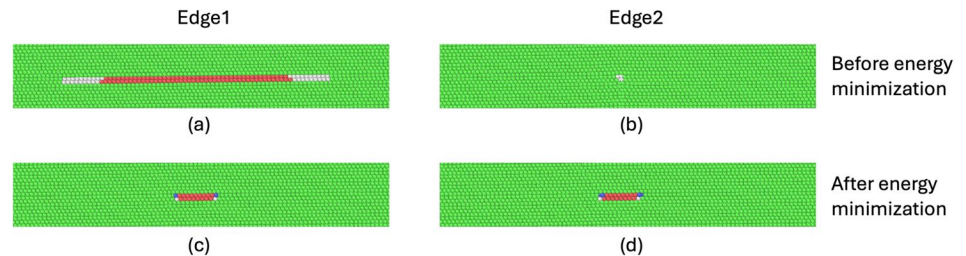


Fig. 10 The same as Fig. 9, but for the MPEA

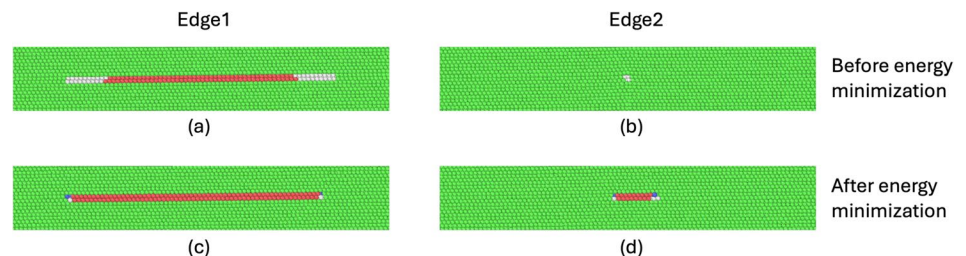
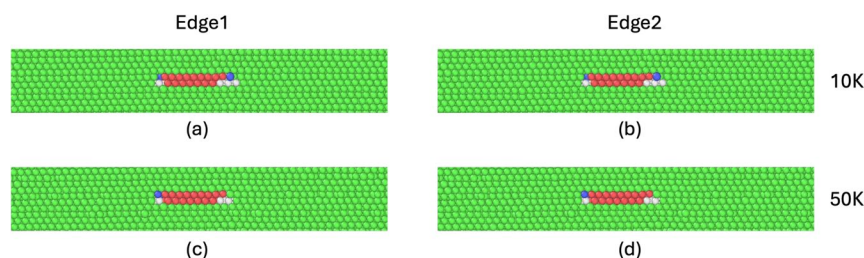


Fig. 11 Edge1 and Edge2 in the MPEA, after dynamic relaxation for 10 ps at 10 K and 50 K, respectively. The color scheme is the same as that in Fig. 9



Conclusion

In this study, we calculate basic structural parameters, GSFEs, and LSRs in $\text{Al}_{0.3}\text{CoCrFeNi}$ MPEA via atomistic simulations. The same properties in Ni are also calculated to provide references. Our analysis shows that the MPEA consistently has a larger lattice parameter than Ni at all temperatures. In both materials, the lattice parameter increases with temperature. Studies of elastic constants demonstrate that while both materials exhibit an initial increase in elastic constants with rising temperature, followed by a decrease in elastic constants.

The examination of GSFE and LSR adds further understanding of the deformation mechanics in the MPEA versus Ni. The lower GSFEs and higher LSR in the MPEA than in Ni suggest that the ductility may be improved in the former without sacrificing the strength [82]. Our findings agree with experiments. For $\text{Al}_{0.3}\text{CoCrFeNi}$, Song et al. [83] reported an ultimate tensile strength (UTS) of 674 MPa with 44% elongation; Zhang et al. [84] found that, after annealing at 700 °C, the alloy exhibits a UTS of 1270 MPa and 11% ductility; Wu et al. [85] observed that deformation at 700 °C resulted in a tensile strength of 390 MPa and approximately 30% ductility. For Ni, Krasilnikov et al. [86] showed that, depending on the annealing and deformation conditions, the UTS ranged from 900 to 1270 MPa, with elongation to fracture varying between 6% and 12%.

The LSR analysis for the same materials reveal an interesting contrast, while Ni displays a higher Peierls stress for the screw dislocation than for the edge dislocation, the MPEA exhibits the opposite, with the edge dislocation facing a greater resistance. This reversal, likely stemming from the alloy's inherent local chemical environment, hints at MPEA's more homogeneous deformation. Notably, while two methods commonly used to create an edge dislocation yield almost the same dislocation structure and Peierls stress in Ni, the same cannot be said for the MPEA. In particular, in the Edge1 configuration, created by stacking two half-crystals together, the initial wide stacking fault in the MPEA cannot be shortened by energy minimization, but can become shorter after finite-temperature dynamic relaxation. Taken together, these findings detail basic structural parameters and dislocation-related properties of an MPEA and highlight its difference from pure metals. Our results

can guide the development of future MPEAs with tailored mechanical properties for extreme environments, such as aerospace and nuclear applications.

Acknowledgements We thank Dr. Wu-Rong Jian for helpful discussions. This work used Bridges-2 at the Pittsburgh Supercomputing Center through allocation # MAT230058 from the Advanced Cyberinfrastructure Coordination Ecosystem: Services & Support (ACCESS) program, which is supported by the National Science Foundation grants #2138259, #2138286, #2138307, #2137603, and #2138296. Some of the computing for this project was performed at the OU Supercomputing Center for Education & Research (OSCAR) at the University of Oklahoma (OU).

Funding A.R. expresses gratitude for receiving the AME Conoco Phillips Scholarship awarded by the University of Oklahoma. Additionally, A.R., S.M., and S.X. are grateful for the startup funds provided by OU.

Data Availability The data presented in this study are openly available at https://github.com/shuozhixu/HEAM_2025

Declarations

Conflict of interest The authors declare no conflict of interest.

References

1. S. Mubassira, W.-R. Jian, S. Xu, Effects of chemical short-range order and temperature on basic structure parameters and stacking fault energies in multi-principal element alloys. *Modelling* **5**(1), 352–366 (2024). <https://doi.org/10.3390/modelling5010019>
2. W. Zhang, P.K. Liaw, Y. Zhang, Science and technology in high-entropy alloys. *Sci. China Mater.* **61**, 2–22 (2018)
3. B. Cantor, I.T.H. Chang, P. Knight, A.J.B. Vincent, Microstructural development in equiatomic multicomponent alloys. *Mater. Sci. Eng., A* **375–377**, 213–218 (2004). <https://doi.org/10.1016/j.msea.2003.10.257>. (Accessed 2023-12-11)
4. J.-W. Yeh, S.-K. Chen, S.-J. Lin, J.-Y. Gan, T.-S. Chin, T.-T. Shun, C.-H. Tsau, S.-Y. Chang, Nanostructured high-entropy alloys with multiple principal elements: novel alloy design concepts and outcomes. *Adv. Eng. Mater.* **6**(5), 299–303 (2004). <https://doi.org/10.1002/adem.200300567>. (Accessed 2023-12-11)
5. Y. Zhang, T.T. Zuo, Z. Tang, M.C. Gao, K.A. Dahmen, P.K. Liaw, Z.P. Lu, Microstructures and properties of high-entropy alloys. *Prog. Mater. Sci.* **61**, 1–93 (2014). <https://doi.org/10.1016/j.pmatsci.2013.10.001>
6. M.-H. Tsai, J.-W. Yeh, High-entropy alloys: a critical review. *Mater. Res. Lett.* **2**(3), 107–123 (2014). <https://doi.org/10.1080/21663831.2014.912690>
7. Y. Zhang, T. Zuo, Y. Cheng, P.K. Liaw, High-entropy alloys with high saturation magnetization, electrical resistivity and malleability. *Sci. Rep.* **3**(1), 1455 (2013)

8. B. Gludovatz, A. Hohenwarter, D. Catoor, E.H. Chang, E.P. George, R.O. Ritchie, A fracture-resistant high-entropy alloy for cryogenic applications. *Science* **345**(6201), 1153–1158 (2014). <https://doi.org/10.1126/science.1254581>
9. I.R. Jamil, A.M. Mustaqim, M. Islam, M.S.H. Thakur, M.N. Hasan, Effect of powder bed fusion process parameters on microstructural and mechanical properties of fecnri mea: an atomistic study. *Met. Mater. Int.* **29**(3), 659–673 (2023)
10. M.A. Hemphill, T. Yuan, G.Y. Wang, J.W. Yeh, C.W. Tsai, A. Chuang, P.K. Liaw, Fatigue behavior of $\text{Al}_{0.5}\text{CoCrCuFeNi}$ high entropy alloys. *Acta Mater.* **60**(16), 5723–5734 (2012). <https://doi.org/10.1016/j.actamat.2012.06.046>
11. A. Kumar, A. Singh, A. Suhane, Mechanically alloyed high entropy alloys: existing challenges and opportunities. *J. Market. Res.* **17**, 2431–2456 (2022). <https://doi.org/10.1016/j.jmrt.2022.01.141>
12. Z. Wang, S. Zhang, Research and application progress of high-entropy alloys. *Coatings* **13**(11), 1916 (2023). <https://doi.org/10.3390/coatings13111916>
13. S. Mubassira, M. Fani, A. Raj, C. Hirt, R.S. Brinlee, A. Poozesh, W.-R. Jian, S.Z. Chavoshi, C. Lee, S. Xu, Chemical short-range order and its influence on selected properties of non-dilute random alloys. *Comput. Mater. Sci.* **248**, 113587 (2025). <https://doi.org/10.1016/j.commatsci.2024.113587>. (Accessed 2024-12-09)
14. C. Li, J.C. Li, M. Zhao, Q. Jiang, Effect of aluminum contents on microstructure and properties of $\text{Al}_x\text{CoCrFeNi}$ alloys. *J. Alloy. Compd.* **504**, 515–518 (2010). <https://doi.org/10.1016/j.jallcom.2010.03.111>
15. A. Sharma, P. Singh, D.D. Johnson, P.K. Liaw, G. Balasubramanian, Atomistic clustering-ordering and high-strain deformation of an $\text{Al}_{0.1}\text{CrCoFeNi}$ high-entropy alloy. *Sci. Rep.* **6**(1), 31028 (2016)
16. D. Li, C. Li, T. Feng, Y. Zhang, G. Sha, J.J. Lewandowski, P.K. Liaw, Y. Zhang, High-entropy $\text{Al}_{0.3}\text{CoCrFeNi}$ alloy fibers with high tensile strength and ductility at ambient and cryogenic temperatures. *Acta Mater.* **123**, 285–294 (2017)
17. Y.X. Zhuang, H.D. Xue, Z.Y. Chen, Z.Y. Hu, J.C. He, Effect of annealing treatment on microstructures and mechanical properties of FeCoNiCuAl high entropy alloys. *Mater. Sci. Eng., A* **572**, 30–35 (2013). <https://doi.org/10.1016/j.msea.2013.01.081>
18. H.F. Sheng, M. Gong, L.M. Peng, Microstructural characterization and mechanical properties of an $\text{Al}_{0.5}\text{CoCrFeCuNi}$ high-entropy alloy in as-cast and heat-treated/quenched conditions. *Mater. Sci. Eng., A* **567**, 14–20 (2013). <https://doi.org/10.1016/j.msea.2013.01.006>
19. J.M. Park, J. Moon, J.W. Bae, M.J. Jang, J. Park, S. Lee, H.S. Kim, Strain rate effects of dynamic compressive deformation on mechanical properties and microstructure of CoCrFeMnNi high-entropy alloy. *Mater. Sci. Eng., A* **719**, 155–163 (2018). <https://doi.org/10.1016/j.msea.2018.02.031>
20. J.-W. Yeh, S.-Y. Chang, Y.-D. Hong, S.-K. Chen, S.-J. Lin, Anomalous decrease in x-ray diffraction intensities of $\text{Cu-Ni-Al-Co-Cr-Fe-Si}$ alloy systems with multi-principal elements. *Mater. Chem. Phys.* **103**(1), 41–46 (2007). <https://doi.org/10.1016/j.matchemphys.2007.01.003>
21. Y.-L. Chen, Y.-H. Hu, C.-A. Hsieh, J.-W. Yeh, S.-K. Chen, Competition between elements during mechanical alloying in an octonary multi-principal-element alloy system. *J. Alloy. Compd.* **481**(1), 768–775 (2009). <https://doi.org/10.1016/j.jallcom.2009.03.087>
22. W.-R. Wang, W.-L. Wang, S.-C. Wang, Y.-C. Tsai, C.-H. Lai, J.-W. Yeh, Effects of Al addition on the microstructure and mechanical property of $\text{Al}_x\text{CoCrFeNi}$ high-entropy alloys. *Intermetallics* **26**, 44–51 (2012). <https://doi.org/10.1016/j.intermet.2012.03.005>
23. A. Sharma, G. Balasubramanian, Dislocation dynamics in $\text{Al}_{0.1}\text{CoCrFeNi}$ high-entropy alloy under tensile loading. *Intermetallics* **91**, 31–34 (2017). <https://doi.org/10.1016/j.intermet.2017.08.004>
24. T.-T. Shun, Y.-C. Du, Microstructure and tensile behaviors of FCC $\text{Al}_{0.3}\text{CoCrFeNi}$ high entropy alloy. *J. Alloy. Compd.* **479**(1), 157–160 (2009). <https://doi.org/10.1016/j.jallcom.2008.12.088>
25. C.-M. Lin, H.-L. Tsai, Evolution of microstructure, hardness, and corrosion properties of high-entropy $\text{Al}_{0.5}\text{CoCrFeNi}$ alloy. *Intermetallics* **19**(3), 288–294 (2011). <https://doi.org/10.1016/j.intermet.2010.10.008>
26. Y.-X. Liu, C.-Q. Cheng, J.-L. Shang, R. Wang, P. Li, J. Zhao, Oxidation behavior of high-entropy alloys $\text{Al}_x\text{CoCrFeNi}$ ($x=0.15, 0.4$) in supercritical water and comparison with hr3c steel. *Trans. Nonferr. Metals Soc. China* **25**(4), 1341–1351 (2015). [https://doi.org/10.1016/S1003-6326\(15\)63733-5](https://doi.org/10.1016/S1003-6326(15)63733-5)
27. Y. Zhang, X. Yang, P. Liaw, Alloy design and properties optimization of high-entropy alloys. *JOM* **64**, 830–838 (2012)
28. A. Gali, E.P. George, Tensile properties of high- and medium-entropy alloys. *Intermetallics* **39**, 74–78 (2013). <https://doi.org/10.1016/j.intermet.2013.03.018>
29. F. Otto, A. Dlouhý, C. Somsen, H. Bei, G. Eggeler, E.P. George, The influences of temperature and microstructure on the tensile properties of a CoCrFeMnNi high-entropy alloy. *Acta Mater.* **61**(15), 5743–5755 (2013)
30. M. Seifi, D. Li, Z. Yong, P.K. Liaw, J.J. Lewandowski, Fracture toughness and fatigue crack growth behavior of as-cast high-entropy alloys. *JOM* **67**, 2288–2295 (2015)
31. L. Li, H. Chen, Q. Fang, J. Li, F. Liu, Y. Liu, P.K. Liaw, Effects of temperature and strain rate on plastic deformation mechanisms of nanocrystalline high-entropy alloys. *Intermetallics* **120**, 106741 (2020)
32. D. Li, Y. Zhang, The ultrahigh charpy impact toughness of forged $\text{Al}_x\text{CoCrFeNi}$ high entropy alloys at room and cryogenic temperatures. *Intermetallics* **70**, 24–28 (2016). <https://doi.org/10.1016/j.intermet.2015.11.002>
33. S. Liu, Y. Wei, The gaussian distribution of lattice size and atomic level heterogeneity in high entropy alloys. *Extreme Mech. Lett.* **11**, 84–88 (2017). <https://doi.org/10.1016/j.eml.2016.10.007>
34. R. Liu, J. Tang, J. Jiang, X. Li, Y. Wei, Stacking fault induced hardening and grain size effect in nanocrystalline conicfemn high-entropy alloy. *Extreme Mech. Lett.* **56**, 101875 (2022). <https://doi.org/10.1016/j.eml.2022.101875>
35. S. Chen, J. Qiao, H. Diao, T. Yang, J. Poplawsky, W. Li, F. Meng, Y. Tong, L. Jiang, P.K. Liaw, Y. Gao, Extraordinary creep resistance in a non-equiatomic high-entropy alloy from the optimum solid-solution strengthening and stress-assisted precipitation process. *Acta Mater.* **244**, 118600 (2023). <https://doi.org/10.1016/j.actamat.2022.118600>
36. Y. Chang, Z. Bai, X. Guo, J. Ren, J. Li, H. Xue, X. Lu, Study on composition optimization and deformation mechanisms of non-equiatomic nicofe medium entropy alloys. *Mater. Today Commun.* **45**, 112305 (2025). <https://doi.org/10.1016/j.mtcomm.2025.112305>
37. J. Li, Q. Fang, B. Liu, Y. Liu, Y. Liu, Mechanical behaviors of AlCrFeCuNi high-entropy alloys under uniaxial tension via molecular dynamics simulation. *RSC Adv.* **6**(80), 76409–76419 (2016)
38. Y. Afkham, M. Bahramyan, R.T. Mousavian, D. Brabazon, Tensile properties of AlCrCoFeCuNi glassy alloys: a molecular dynamics simulation study. *Mater. Sci. Eng., A* **698**, 143–151 (2017). <https://doi.org/10.1016/j.msea.2017.05.057>
39. R. Ishraaq, S.M. Nahid, S. Chhetri, O. Gautam, A.M. Afsar, A molecular dynamics investigation for predicting the optimum fiber radius and the effect of various parameters on the mechanical properties of carbon nanotube reinforced iron composite. *Comput. Mater. Sci.* **174**, 109486 (2020). <https://doi.org/10.1016/j.commat.2019.109486>

40. S. Chhetri, E. Moraes, M. Naghibolhosseini, M. Zayernouri, A comparative study of dislocation dynamics in ductile and brittle crystalline materials. In: 2023 International Conference on Modeling, Simulation & Intelligent Computing (MoSiCom), pp. 438–441 (2023). <https://doi.org/10.1109/MoSiCom59118.2023.10458756>
41. M. Li, J. Gazquez, A. Borisevich, R. Mishra, K.M. Flores, Evaluation of microstructure and mechanical property variations in $\text{Al}_x\text{CoCrFeNi}$ high entropy alloys produced by a high-throughput laser deposition method. *Intermetallics* **95**, 110–118 (2018). <https://doi.org/10.1016/j.intermet.2018.01.021>. (Accessed 2024-12-28)
42. F. Wei, S. Wei, K.B. Lau, W.H. Teh, J.J. Lee, H.L. Seng, C.C. Tan, P. Wang, U. Ramamurty, Compositionally graded $\text{Al}_x\text{CoCrFeNi}$ high-entropy alloy manufactured by laser powder bed fusion. *Materialia* **21**, 101308 (2022). <https://doi.org/10.1016/j.mtla.2021.101308>. (Accessed 2024-12-28)
43. Z. Sun, C. Shi, C. Liu, H. Shi, J. Zhou, The effect of short-range order on mechanical properties of high entropy alloy $\text{Al}_{0.3}\text{CoCrFeNi}$. *Mater. Design* **223**, 111214 (2022). <https://doi.org/10.1016/j.matdes.2022.111214>
44. M.A.A. Hasan, S. Shin, P.K. Liaw, Short-range order effects on the thermodynamic behavior of $\text{Al}_x\text{CoCrFeNi}$ high-entropy alloys. *Comput. Mater. Sci.* **239**, 112980 (2024). <https://doi.org/10.1016/j.commatsci.2024.112980>
45. R. Pasianot, D. Farkas, Atomistic modeling of dislocations in a random quinary high-entropy alloy. *Comput. Mater. Sci.* **173**, 109366 (2020). <https://doi.org/10.1016/j.commatsci.2019.109366>. (Accessed 2020-01-23)
46. S. Xu, Y. Su, W.-R. Jian, I.J. Beyerlein, Local slip resistances in equal-molar MoNbTi multi-principal element alloy. *Acta Mater.* **202**, 68–79 (2021). <https://doi.org/10.1016/j.actamat.2020.10.042>. (Accessed 2020-11-03)
47. M.S. Nitol, M.J. Echeverria, K. Dang, M.I. Baskes, S.J. Fensin, New modified embedded-atom method interatomic potential to understand deformation behavior in VNbTaTiZr refractory high entropy alloy. *Comput. Mater. Sci.* **237**, 112886 (2024). <https://doi.org/10.1016/j.commatsci.2024.112886>. (Accessed 2024-10-19)
48. R.A. Romero, S. Xu, W.-R. Jian, I.J. Beyerlein, C.V. Ramana, Atomistic simulations of the local slip resistances in four refractory multi-principal element alloys. *Int. J. Plast.* **149**, 103157 (2022). <https://doi.org/10.1016/j.ijplas.2021.103157>. (Accessed 2022-12-26)
49. A.P. Thompson, H.M. Aktulga, R. Berger, D.S. Bolintineanu, W.M. Brown, P.S. Crozier, P.J. In't Veld, A. Kohlmeyer, S.G. Moore, T.D. Nguyen, R. Shan, M.J. Stevens, J. Tranchida, C. Trott, S.J. Plimpton, LAMMPS - a flexible simulation tool for particle-based materials modeling at the atomic, meso, and continuum scales. *Comp. Phys. Commun.* **271**, 108171 (2022). <https://doi.org/10.1016/j.cpc.2021.108171>
50. P. Hirel, AtomsK: a tool for manipulating and converting atomic data files. *Comput. Phys. Commun.* **197**, 212–219 (2015). <https://doi.org/10.1016/j.cpc.2015.07.012>
51. A. Stukowski, Visualization and analysis of atomistic simulation data with ovito—the open visualization tool. *Modell. Simul. Mater. Sci. Eng.* **18**(1), 015012 (2009). <https://doi.org/10.1088/0965-0393/18/1/015012>
52. M.S. Daw, M.I. Baskes, Embedded-atom method: derivation and application to impurities, surfaces, and other defects in metals. *Phys. Rev. B* **29**(12), 6443 (1984)
53. D. Farkas, A. Caro, Model interatomic potentials for Fe-Ni-Cr-Co-Al high-entropy alloys. *J. Mater. Res.* **35**(22), 3031–3040 (2020). <https://doi.org/10.1557/jmr.2020.294>
54. X.W. Zhou, R.A. Johnson, H.N.G. Wadley, Misfit-energy-increasing dislocations in vapor-deposited CoFe/NiFe multilayers. *Phys. Rev. B* **69**, 144113 (2004). <https://doi.org/10.1103/PhysRevB.69.144113>
55. R. Babicheva, A. Jarlöv, H. Zheng, S. Dmitriev, E. Korznikova, M. Ling Sharon Nai, U. Ramamurty, K. Zhou, Effect of short-range ordering and grain boundary segregation on shear deformation of CoCrFeNi high-entropy alloys with Al addition. *Comput. Mater. Sci.* **215**, 111762 (2022). <https://doi.org/10.1016/j.commatsci.2022.111762>
56. X. Ma, W. Zhang, F. Zhu, L. Song, Q. Zhang, The effect of Al in $\text{Al}_{0.3}\text{CoCrFeNi}$ alloy on the damage accumulation at different temperatures. *J. Nucl. Mater.* **600**, 155283 (2024). <https://doi.org/10.1016/j.jnucmat.2024.155283>
57. J. Kong, G. Luo, Y. Tian, C. Du, Atomic insight into tribological behavior of AlCoCrFeNi high entropy alloy at various nano-scratching conditions. *J. Market. Res.* **27**, 7293–7303 (2023). <https://doi.org/10.1016/j.jmrt.2023.11.150>
58. Z. Sun, C. Shi, L. Gao, S. Lin, W. Li, Thermal physical properties of high entropy alloy $\text{Al}_{0.3}\text{CoCrFeNi}$ at elevated temperatures. *J. Alloy. Compd.* **901**, 163554 (2022). <https://doi.org/10.1016/j.jallcom.2021.163554>
59. G. Li, L. Yuan, J. Li, M. Zhang, D. Li, Effect of Al related chemical short-range order on the irradiation resistance of $\text{Al}_{0.5}\text{CoCrFeNi}$ multi-principal element alloy: A molecular dynamics simulation. *Mater. Today Commun.* **38**, 108302 (2024). <https://doi.org/10.1016/j.mtcomm.2024.108302>
60. Y. Zhang, Y.J. Zhou, J.P. Lin, G.L. Chen, P.K. Liaw, Solid-solution phase formation rules for multi-component alloys. *Adv. Eng. Mater.* **10**(6), 534–538 (2008)
61. W.-R. Jian, S. Xu, I.J. Beyerlein, On the significance of model design in atomistic calculations of the peierls stress in nb. *Comput. Mater. Sci.* **188**, 110150 (2021). <https://doi.org/10.1016/j.commatsci.2020.110150>
62. J.R. Ray, A. Rahman, Statistical ensembles and molecular dynamics studies of anisotropic solids. *J. Chem. Phys.* **80**(9), 4423–4428 (1984). <https://doi.org/10.1063/1.447221>. (Accessed 2023-12-29)
63. S. Xu, S.Z. Chavoshi, Y. Su, On calculations of basic structural parameters in multi-principal element alloys using small atomistic models. *Comput. Mater. Sci.* **202**, 110942 (2022). <https://doi.org/10.1016/j.commatsci.2021.110942>. (Accessed 2021-10-12)
64. S. Xu, J.Y. Cheng, Z. Li, N.A. Mara, I.J. Beyerlein, Phase-field modeling of the interactions between an edge dislocation and an array of obstacles. *Comput. Meth. Appl. Mech. Eng.* **389**, 114426 (2022). <https://doi.org/10.1016/j.cma.2021.114426>. (Accessed 2022-01-29)
65. E.P. George, D. Raabe, R.O. Ritchie, High-entropy alloys. *Nat. Rev. Mater.* **4**(8), 515–534 (2019)
66. T.E. Mitchell, Slip in body-centred cubic crystals. *Philos. Mag.* **17**(150), 1169–1194 (1968). <https://doi.org/10.1080/14786436808223194>
67. S.J. Zhou, A.E. Carlsson, R. Thomson, Dislocation core-core interaction and peierls stress in a model hexagonal lattice. *Phys. Rev. B* **49**, 6451–6456 (1994). <https://doi.org/10.1103/PhysRevB.49.6451>
68. X. Wang, S. Xu, W.-R. Jian, X.-G. Li, Y. Su, I.J. Beyerlein, Generalized stacking fault energies and peierls stresses in refractory body-centered cubic metals from machine learning-based interatomic potentials. *Comput. Mater. Sci.* **192**, 110364 (2021). <https://doi.org/10.1016/j.commatsci.2021.110364>
69. A. Pourattar, M. Habibi Parsa, R. Roumina, A study on the role of construction methods of an edge dislocation on final arrangements of atoms via MD simulations. *J. Mater. Res.* **39**, 3139–3154 (2024). <https://doi.org/10.1557/s43578-024-01451-0>. (Accessed 2024-11-07)
70. Y.N. Osetsyky, D.J. Bacon, An atomic-level model for studying the dynamics of edge dislocations in metals. *Modelling Simul.*

- Mater. Sci. Eng. **11**(4), 427–446 (2003). <https://doi.org/10.1088/0965-0393/11/4/302>. (Accessed 2016-01-03)
71. D. Rodney, G. Martin, Dislocation pinning by small interstitial loops: a molecular dynamics study. *Phys. Rev. Lett.* **82**(16), 3272–3275 (1999). <https://doi.org/10.1103/PhysRevLett.82.3272>. (Accessed 2024-11-07)
 72. P. Khanikar, A. Kumar, A. Subramaniam, Image forces on edge dislocations: a revisit of the fundamental concept with special regard to nanocrystals. *Philos. Mag.* **91**(5), 730–750 (2011). <https://doi.org/10.1080/14786435.2010.529089>. (Accessed 2024-11-07)
 73. Y. Su, S. Xu, I.J. Beyerlein, Density functional theory calculations of generalized stacking fault energy surfaces for eight face-centered cubic transition metals. *J. Appl. Phys.* **126**(10), 105112 (2019). <https://doi.org/10.1063/1.5115282>. (Accessed 2019-09-13)
 74. Z. Wei, T. Xia, J. Ma, W. Feng, J. Dai, Q. Wang, P. Yan, Investigation of the lattice expansion for Ni nanoparticles. *Mater. Charact.* **58**(10), 1019–1024 (2007). <https://doi.org/10.1016/j.matchar.2006.08.004>
 75. H. Warlimont, W. Martienssen, *Springer Handbook of Materials Data*. Springer Handbooks. (Springer, 2018). <https://books.google.com/books?id=rli8tAEACAAJ>
 76. A. Zaddach, C. Niu, C. Koch, D. Irving, Mechanical properties and stacking fault energies of NiFeCrCoMn high-entropy alloy. *JOM* **65**, 1780–1789 (2013)
 77. Y.P. Varshni, Temperature dependence of the elastic constants. *Phys. Rev. B* **2**(10), 3952–3958 (1970). <https://doi.org/10.1103/PhysRevB.2.3952>. (Accessed 2025-01-17)
 78. T. Çağın, G. Dereli, M. Uludoğan, M. Tomak, Thermal and mechanical properties of some fcc transition metals. *Phys. Rev. B* **59**(5), 3468–3473 (1999). <https://doi.org/10.1103/PhysRevB.59.3468>. (Accessed 2025-01-17)
 79. Z. Wu, H. Bei, G.M. Pharr, E.P. George, Temperature dependence of the mechanical properties of equiatomic solid solution alloys with face-centered cubic crystal structures. *Acta Mater.* **81**, 428–441 (2014). <https://doi.org/10.1016/j.actamat.2014.08.026>. (Accessed 2024-10-14)
 80. S. Xu, J.R. Mianroodi, A. Hunter, B. Svendsen, I.J. Beyerlein, Comparative modeling of the disregistry and Peierls stress for dissociated edge and screw dislocations in Al. *Int. J. Plast.* **129**, 102689 (2020). <https://doi.org/10.1016/j.ijplas.2020.102689>. (Accessed 2020-02-04)
 81. T. Wang, J. Li, M. Wang, C. Li, Y. Su, S. Xu, X.-G. Li, Unraveling dislocation-based strengthening in refractory multi-principal element alloys. *npj Comput. Mater.* **10**(1), 143 (2024). <https://doi.org/10.1038/s41524-024-01330-6>. (Accessed 2024-10-19)
 82. F. Shuang, L. Laurenti, P. Dey, Standard deviation in maximum restoring force controls the intrinsic strength of face-centered cubic multi-principal element alloys. *Acta Mater.* **282**, 120508 (2025). <https://doi.org/10.1016/j.actamat.2024.120508>. (Accessed 2024-11-07)
 83. S. Song, X. Wang, Z. Zhang, X. Ren, Investigation on effect of L1₂ and B2 phases on tensile properties and mechanisms of Al_{0.3}CoCrFeNi high entropy alloy through aging treatment. *J. Alloy. Compd.* **1010**, 177435 (2025). <https://doi.org/10.1016/j.jallcom.2024.177435>
 84. K. Zhang, Y. Liu, L. Wu, N. Zhang, L. Li, L. Zhang, H. Yan, P. Hodgson, M. Cai, The effect of the interaction between recrystallization and precipitation on the heterogeneous microstructure and tensile properties in a heavily cold-rolled Al_{0.3}CoCrFeNi high-entropy alloy. *J. Alloy. Compd.* **1010**, 178241 (2025). <https://doi.org/10.1016/j.jallcom.2024.178241>
 85. Y. Wu, J. Brechtel, C. Li, P.K. Liaw, G. Geng, Y. Zhang, Serration behavior and brittle phase-induced mechanical transitions in wrought Al_{0.3}CoCrFeNi high-entropy alloy from 100 °C to 800 °C. *Mater. Sci. Eng., A* **932**, 148261 (2025). <https://doi.org/10.1016/j.msea.2025.148261>
 86. N. Krasilnikov, W. Lojkowski, Z. Pakiel, R. Valiev, Tensile strength and ductility of ultra-fine-grained nickel processed by severe plastic deformation. *Mater. Sci. Eng., A* **397**(1), 330–337 (2005). <https://doi.org/10.1016/j.msea.2005.03.001>

Springer Nature or its licensor (e.g. a society or other partner) holds exclusive rights to this article under a publishing agreement with the author(s) or other rightsholder(s); author self-archiving of the accepted manuscript version of this article is solely governed by the terms of such publishing agreement and applicable law.